*Article*

# Geomorphological Evolution in the Tidal Flat of a Macro-Tidal Muddy Estuary, Hangzhou Bay, China, over the Past 30 Years

Li Li [1,2], Fangzhou Shen [1], Yuezhang Xia [1,2,*], Haijing Shi [3], Nan Wang [4], Zhiguo He [1,2] and Kai Gao [1]

1   Ocean College & Ocean Research Center of Zhoushan, Zhejiang University, Zhoushan 316021, China; lilizju@zju.edu.cn (L.L.); 12034048@zju.edu.cn (F.S.); hezhiguo@zju.edu.cn (Z.H.); 22334163@zju.edu.cn (K.G.)
2   Key Laboratory of Offshore Geotechnical and Material Engineering of Zhejiang Province, Zhejiang University, Hangzhou 310058, China
3   Institute of Soil and Water Conservation, Northwest A&F University, Xianyang 712100, China; shihaijingcn@nwafu.edu.cn
4   Marine Science and Technology College, Zhejiang Ocean University, Zhoushan 316022, China; wangnan@zjou.edu.cn
*   Correspondence: yzxia@zju.edu.cn

**Abstract:** Tidal flat plays an important role in coastal development because of its ecological and spatial resources. We take the southern tidal flat in the macro-tidal turbid Hangzhou Bay as an example to study the long-term (1990–2020) evolution of the muddy tidal flat, using remote sensing data and field observational data. The detailed bathymetric elevation of the tidal flat is obtained, using remote sensing images of Landsat and Sentinel-2, combined with the real-time kinematic (RTK) data. The correlation coefficient between the remote sensing data and the RTK data is 0.73. The tidal flat and vegetation areas are affected by reclamation. The total tidal flat area decreased by 467.78 km$^2$. The vegetation area declined from 64.98 km$^2$ in 2000 to 13.41 km$^2$ in 2015 and recovered to 41.62 km$^2$ in 2020. The largest change in tidal flat slope occurs in the eastern and western sides of the tidal flat, compared with the wide middle part. The total length of tidal creeks decreased to 45.95 km in 2005 and then increased to 105.83 km in 2020. The middle- and low-grade tidal creeks accounted for 91.4%, with a curvature slightly larger than 1 in 2020. High-grade tidal creeks occur inside the vegetation areas, with less bending and fewer branch points. Vegetation promotes the development of tidal creeks but limits the lateral swing and bifurcation. These results provide a basis for the management of global tidal flat resources and ecosystems.

**Keywords:** tidal flat; vegetation; tidal creek; bathymetry elevation; variation; Hangzhou Bay

## 1. Introduction

Tidal flats, widely distributed in macro-tidal estuaries and coastal areas, play an important role in marine ecosystems and coastal economies [1]. The various geomorphology, complex hydrodynamic conditions, and diverse biological resources make the morphology of tidal flats important in marine economy and coastal safety [2–4]. Tidal flats carry a wide range of offshore engineering construction, reclamation, and other human activities [5]. Typical marine carbon sink systems such as wetlands and mangroves are closely related to tidal flats. Understanding the characteristics and evolution of tidal flats supports coastal resources and ecosystems and contributes to blue carbon management.

Tidal flat bathymetry is a key parameter for coastal disaster management. Obtaining accurate bathymetry has received continuous attention [6–8]. Field observation is conducted to obtain the bathymetry data using a 3D (three-dimensional) terrain laser scanner or unmanned aerial vehicle scanning during spring low slack water when the tidal flat is non-submerged. In recent years, the calculation of shallow water Sentinel-2 bathymetry based on remote sensing data has been developed using ICESat-2 Photon-Counting Lidar combined with classical wave theory [9], or ICESat-2 Laser Altimetry combined with

Sentinel-2 Imagery [8]. Hsu et al. [7] provided a semi-empirical scheme for bathymetric mapping in shallow water using ICESat-2 and Sentinel-2. Field-based RTK (real-time kinematic) data can serve as a substitute when the elevation footprints of the satellite do not cover the study area. Benefiting from the advantages of image-pattern recognition, deep learning is used to overcome complex imaging conditions [6].

Vegetation and tidal creeks are important factors in tidal flat evolution, which influence the material exchange and provide coastal ecosystem and safety. Vegetation is effective in reducing typhoon waves [10], and thus, it is essential for tidal flat geomorphological evolution [11]. Due to the water retardation by vegetation [12,13], tidal creeks exhibit increased bifurcation, grade, and curvature from coastal to inland [12,14]. An increase in vegetation enhances bed roughness, promotes tidal creek development, and increases tidal creek density [15]. However, excessive vegetation, such as the severe invasion of *Spartina alterniflora*, results in strong retention and wave-dampening effects, leading in the shallowing or even disappearance of tidal creeks [16]. The higher the vegetation coverage rate in tidal flats, the lower the tidal creek density [17]. Vegetation constrains the lateral development and swing of tidal trenches. High-grade tidal creeks tend to have fewer bifurcations [17]. There is a negative correlation between the length of the tidal creek and vegetation coverage due to high salinity [18]. The expansion of *S. alterniflora* is an important factor that affects the degradation of the tidal creek and plant communities [19,20]. Therefore, the relationship between tidal flat evolution, tidal creek development, and vegetation is complicated; the coupling effects of vegetation species, density, distribution patterns, and hydrological factors should be considered [21–23].

Human activities influence the development of tidal flats [24]. Tidal flat reclamation completely or partially changes the local coastal landform, cuts off the material exchange, and then affects waves, tides, and sediments [25]. After reclamation, a new stability of tidal flat topography, tidal creeks, and vegetation [26] was formed [27]. For example, in the Yellow River Delta (YRD), tidal flat reclamation truncated the upstream tidal creek. Subsequently, the tidal creek changed its shape and increased its curvature and density. A new stability was formed to maintain drainage efficiency. Therefore, reclamation in the YRD tidal flat promotes the development of tidal creek curvature [24]. The large-scale reclamation activities of the eastern Chongming tidal flat in the Changjiang River Estuary have gradually disappeared from the tidal creek system in the northeast [28]. Coastal engineering, such as dikes, also affects hydrodynamics and erosion and deposition of sediments, resulting in tidal flat evolution [29], but usually with a threshold limitation [30]. Thus, scale properties should be considered in the study of the impact of human activities on tidal flats, that is, the rapid and severe impact of intense human activities on tidal flats may self-recover, unless the effect is too large to exceed scale invariance [31].

Many studies have shown that tidal flats affect estuarine dynamics, such as hydrodynamics, sediment dynamics, and tidal channels [32,33]. However, detailed information on tidal flats and their annual variations is largely unknown [34–36]. Rapidly measuring the detailed topography of tidal flats is important for coastal management and safety, and clearly knowing the evolution of tidal flats supports the planning of coastal zones [8]. This study uses the southern tidal flat in the HZB as an example to investigate the characteristics of tidal flat geomorphology (area, altimetry, and tidal creek) using field data and remote sensing data. The spatial and temporal variations in tidal flat characteristics were examined, and the impacts of vegetation and human activity on the tidal creek are discussed. This study promotes a better understanding of the evolution of the tidal flat ecosystem and provides theoretical support for tidal flat management.

## 2. Methodology
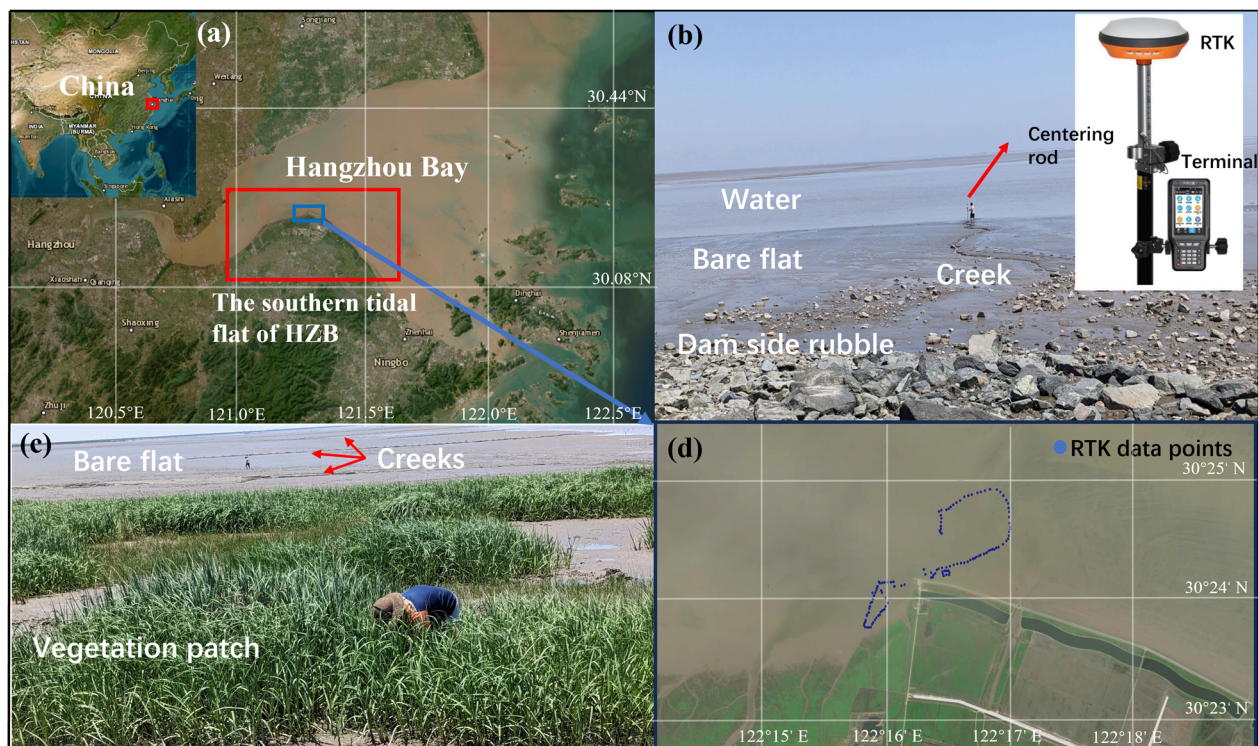
### 2.1. Field Data and Remote Sensing Data

2.1.1. Study Area and Field Data

The southern tidal flat of Hangzhou Bay (HZB) is approximately 281.49 km$^2$ and accounts for approximately 25% of the total existing tidal flats in Zhejiang Province and

3.2% of the total existing tidal flats in China [37]. HZB is a typical macro-tidal estuary. Strong tidal wave deformation results in high sediment erosion in tidal flats and banks [38]. The southern tidal flat is a turbid area, as proven by remote sensing and numerical simulation analyses [39–41]. Researchers have analyzed the evolution of this tidal flat using topographic data or remote sensing images [4,42], as the effects of vegetation on carbon sinks are of particular interest [43]. The tidal flats in HZB are greatly influenced by human activities; for example, a reclamation project changed the hydro-sediment dynamics in and near the tidal flat [44], and the continuous reclamation to the sea and the siltation of tidal flats show a positive feedback mechanism, as shown a by numerical simulation study [45].

We obtained field data from the southern tidal flat of HZB on 10 May 2023. As shown in Figure 1b,c, the southern tidal flat can be divided into a barren flat and a tidal flat with vegetation. The elevation data of the selected field sites in the tidal flat were measured using real-time kinematic (RTK) (Figure 1b). As presented in Figure 1d, the 128 sampling sites were selected to cover the bare flat (80 sites), tidal creek (30 sites), and vegetation area (18 sites). The correlation between the field data and remote sensing data was obtained. The elevation data of the entire tidal flat were then obtained using the remote sensing data and the correlation function. The correlation was a linear function between the orthometric height and inundation frequency.



**Figure 1.** Study area. (**a**) The southern tidal flat of HZB; (**b**,**c**) field observation and RTK instrument; (**d**) observation sites.

### 2.1.2. Remote Sensing Data

We obtained Landsat remote sensing images of the southern tidal flat for 1990, 1995, 2000, 2005, 2010, 2015, and 2020 (Table 1). Landsat 8 Operational Land Imager (OLI) images gathered in 2015 and 2020 were used in the analysis along with Landsat 4–5 TM images from 1990 to 2010.

The remote sensing images were preprocessed using the band composition, geometric calibration, radiation calibration, and atmospheric calibration. To facilitate subsequent geometric calibration, waterlines, and vegetation extraction, we synthesized the images of red, blue, and green bands to obtain the HZB remote sensing image (Figure 2a). Owing to the influence of terrain curvature, sensor position, and other factors, there is a positional

deviation between the object position in the images and its actual position; therefore, we selected clear and distinguishable structures and natural landform feature points as the control points. Finally, we selected 30 control points in HZB, and the root mean square error (RMSE) after calibration was 0.003 (Figure 2b). Because of the interference of external factors, Landsat series satellites produce random and systematic radiation distortions when acquiring and transmitting remote sensing data, which distort images [46]. The Radiometric Calibration tool in ENVI was used to eliminate radiation errors and correct image distortion (Figure 2c). After geometric and radiation calibration, the atmospheric calibration tool was used to eliminate the influence of atmospheric factors (Figure 2d).

**Table 1.** Landsat image data.

| Data Identifier | Date * | Flood/Dry | Cloud Cover (%) | Notes |
|---|---|---|---|---|
| LT51180391990162HAJ00 | 11 June 1990 | Flood | 0.13 | Near high-water level |
| LT51180391990226HAJ00 | 14 August 1990 | Flood | — | |
| LT51180391990338HAJ00 | 4 December 1990 | Dry | — | Near low-water level |
| LT51180391995192HAJ00 | 11 July 1995 | Flood | 0.22 | Near high-water level |
| LT51180391995224HAJ00 | 12 August 1995 | Flood | — | |
| LT51180391995256CLT02 | 13 September 1995 | Flood | 14.27 | Near low-water level |
| LT51180391999043HAJ00 | 12 February 1999 | Dry | 1.37 | Near low-water level |
| LT51180391999091HAJ00 | 1 April 1999 | Normal | 0.46 | |
| LT51180392000158HAJ03 | 6 June 2000 | Flood | 6.12 | Near high-water level |
| LT51180392004201BJC00 | 19 July 2004 | Flood | 14.22 | Near high-water level |
| LT51180392005155BJC00 | 4 June 2005 | Flood | 0.56 | |
| LT51180392005331BJC00 | 27 November 2005 | Dry | — | Near low-water level |
| LT51180392009198BJC00 | 17 July 2009 | Flood | 0.07 | Near high-water level |
| LT51180392010313BJC00 | 9 November 2010 | Dry | — | |
| LT51180392010361BJC00 | 27 December 2010 | Dry | 5.00 | Near low-water level |
| LC81180392015023LGN00 | 23 January 2015 | Dry | 18.80 | Near low-water level |
| LC81180392015071LGN00 | 12 March 2015 | Normal | 2.74 | |
| LC81180392015215LGN00 | 3 August 2015 | Flood | 0.50 | Near high-water level |
| LC81180392020133LGN00 | 12 May 2020 | Flood | 18.01 | Near high-water level |
| LC81180392020229LGN00 | 16 August 2020 | Flood | 9.23 | |
| LC81180392021087LGN00 | 28 March 2021 | Normal | 15.73 | Near low-water level |

* The images are selected in about 5-year intervals, considering the limitations of remote sensing data, and the oceanic and meteorological conditions.

### 2.2. Calculation of Tidal Flat Parameters

2.2.1. Elevation

We used Xu et al.'s [8] method to estimate the tidal flat elevation. The point elevations at the waterline captured from a satellite image were assumed to fall on a contour line and were, therefore, equivalent. Their relative heights are represented by the tide level [47,48]. The remote sensing images of the same area were superimposed, and then the inundation frequencies of the points were calculated (Equation (1)). High-elevation places are much less likely to inundate, implying that a correlation exists between the elevation and inundation frequency. The function relation $f(obsh, inunfre)$ between elevation and the inundation frequency was obtained by correlation analysis. Then, the elevation of the entire tidal flat was calculated (Equation (2)).

$$inunfre = \frac{\sum inundation}{\sum pixel} \tag{1}$$

$$ele = inunfre \cdot f(obsh, inunfre) \tag{2}$$

where *inunfre* is the inundation frequency—that is, the probability that the same point in the superimposed image pixels is identified as submerged. *ele* is the tidal flat elevation.
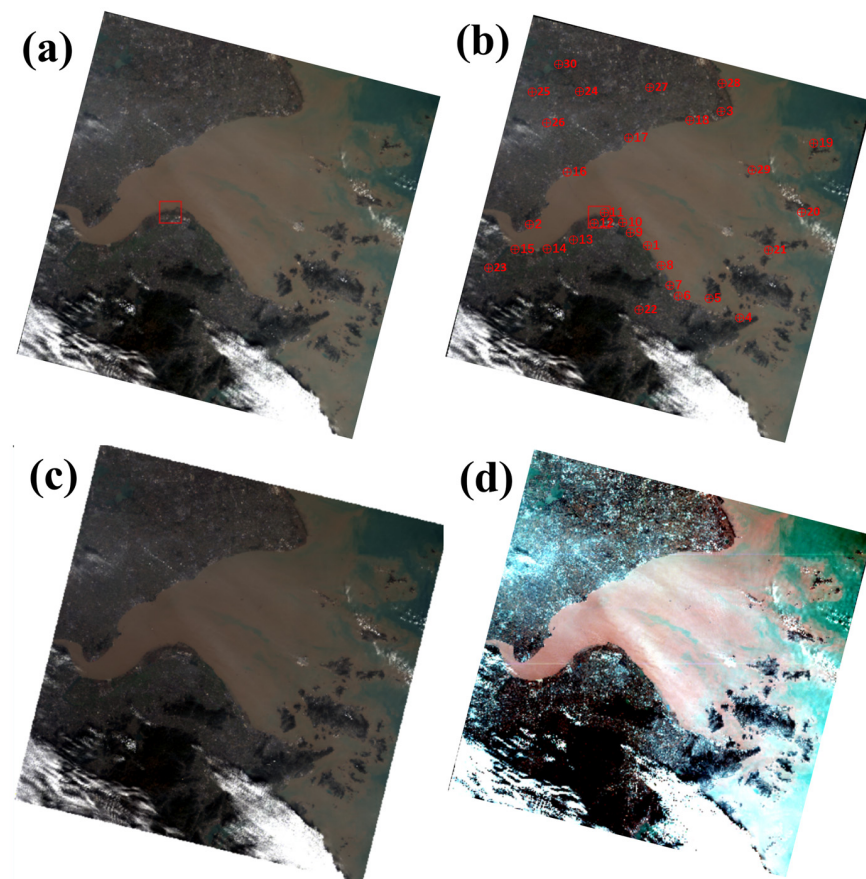
**Figure 2.** Preprocessing of remote sensing image in HZB in 2020. (**a**) Image after band composition; (**b**) image after geometric calibration. Note that the red points are selected control points; (**c**) image after radiation calibration; and (**d**) image after atmospheric calibration.

The elevation data of the ICESat-2 Laser Altimetry can be used in correlation analysis if the footprints of the satellite pass through the study area. In this study, we used the measured field elevation data for analysis. The field data were controlled by using the sigma principle, which is a common method used in statistics for data quality control.

### 2.2.2. Waterline and Areas

A tidal flat refers to the area of inshore flooding between the mean high tide line and the mean low tide line [49]. Tidal flat area extraction methods based on waterlines include the tidal level correction method, the outermost waterline method described in ArcGIS [50], and the eight-division method used for calculating the tide. The tidal flat area can be calculated using the corrected waterline.

Extraction methods for instantaneous waterlines from remote sensing images include visual interpretation, edge detection, threshold segmentation, and object-oriented extraction methods [51–54]. Visual interpretation is the simplest but most human-intensive method for waterline extraction. For coastlines with clear boundaries, such as rocky and artificial coasts, the visual interpretation results are accurate [55].

For muddy coasts with vegetation, edge detection can improve the accuracy of waterlines and reduce noise. The result is generally favorable for mudflats with uncertain boundaries [56]. Hence, an edge detection method combined with a visual interpretation method is used to extract waterlines.

In this study, the mean spring tide low waterline (the mean low water level during spring tides), corrected by the tide level in the TPXO 7.2 tide level prediction model [57], was used as the lower boundary of the tidal flat. For the artificial coast, a seawall was used as the higher boundary of the tidal flat. For the rocky and muddy coast, the mean spring

tide high waterline (the mean high water level during spring tides) corrected by the tide level was used as the higher boundary of the tidal flat [58]. High and low waterlines of the spring tides were obtained by correcting the remote sensing waterlines, and the area between the two lines was regarded as a tidal flat area [59].

### 2.2.3. Slope

The profile morphology discriminant inferential method (PMDI) was used to preliminarily divide the different profile forms of the tidal flat. Then, a suitable fit curve was chosen to calculate the slope. Transverse sections perpendicular to the tidal flat longitudinal direction (along the waterline) were selected with uniform intervals. Three discrete points, the near-land side boundary point $(L_1, H_1)$, offshore side boundary point $(L_2, H_2)$, and middle point $(L_0, H_0)$, were selected on the transverse sections (Figure 3d) [60]. $L$ represents the horizontal distance between the point and the reference origin, and $H$ represents the tidal elevation of the point. The reference origin was set at the corresponding transverse section. Three evenly distributed middle points are sufficient, and additional middle points have little influence on the fitting accuracy of the tidal flat profile [61]. According to $(L_1, H_1)$ and $(L_2, H_2)$, the linear Equation (3) of the tidal flat slope can be constructed to obtain the tidal elevation $H_*$ at the horizontal distance $L_0$. The slope average error is defined as $\Delta H = H_* - H_0$.
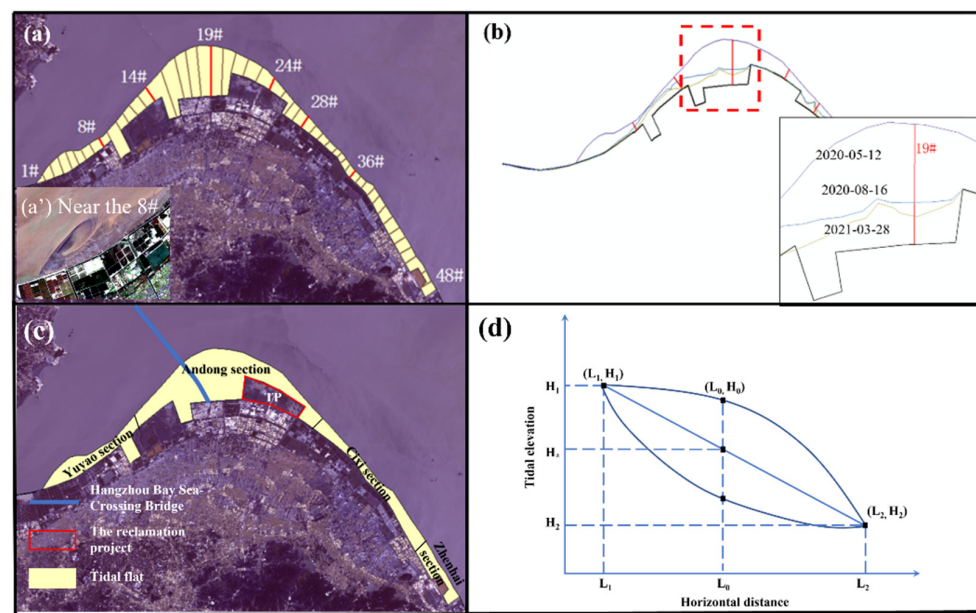


**Figure 3.** (**a**) Sections; (**a'**) the sandbar near the 8# section; (**b**) 19# section and waterlines at three different times; (**c**) tidal flat areas; (**d**) schematic diagram of discrete point selection by PMDI method.

When $|\Delta H| < \frac{Err}{2}$, the tidal flat has a gentle slope profile. Using linear fitting, the following can be obtained:

$$H = kL + h_0 \tag{3}$$

When $\Delta H < -\frac{Err}{2}$ is used, the tidal flat has an erosive convex profile. Using a second-order polynomial fit, the following can be obtained:

$$H = k_1 L^2 + k_2 L + h_0 \tag{4}$$

When $\Delta H > \frac{Err}{2}$, the tidal flat has an erosive concave profile. Using an exponential fit, the following can be obtained:

$$H = \sum_{i=1}^{3} A_i e^{-L/u_i} + h_0 \tag{5}$$

where, $h_0$, $k_i$, $A_i$, and $u_i$ are the constants of the fitting function.

*Err* is the profile slope control error, usually 0.15–0.20 m and 1 to 1.33 times the RMSE of tidal level harmonic analysis [23]. The fitting results of these formulas were close to the actual tidal flat profile [59], and the slope was calculated using Equation (6).

$$S = \frac{\sum_{i=1}^{n} \frac{h_{i-1} - h_i}{L_i} S_i}{\sum_{i=1}^{n} S_i} \qquad (6)$$

where $n$ is the number of discrete points, $h_i$ is the tidal elevation at these points, $L_i$ is the horizontal distance, and $S_i$ is the horizontal distance between the points.

In this study, 48 sections (1#–48#) were selected with a 2.2 km interval (Figure 3a). The sections intersected the waterlines at three points (Figure 3b). Six sections (8#, 14#, 19#, 24#, 28#, and 36#), with obvious topographic relief or a large width, were selected for topographic fitting and analysis (Figure 3a).
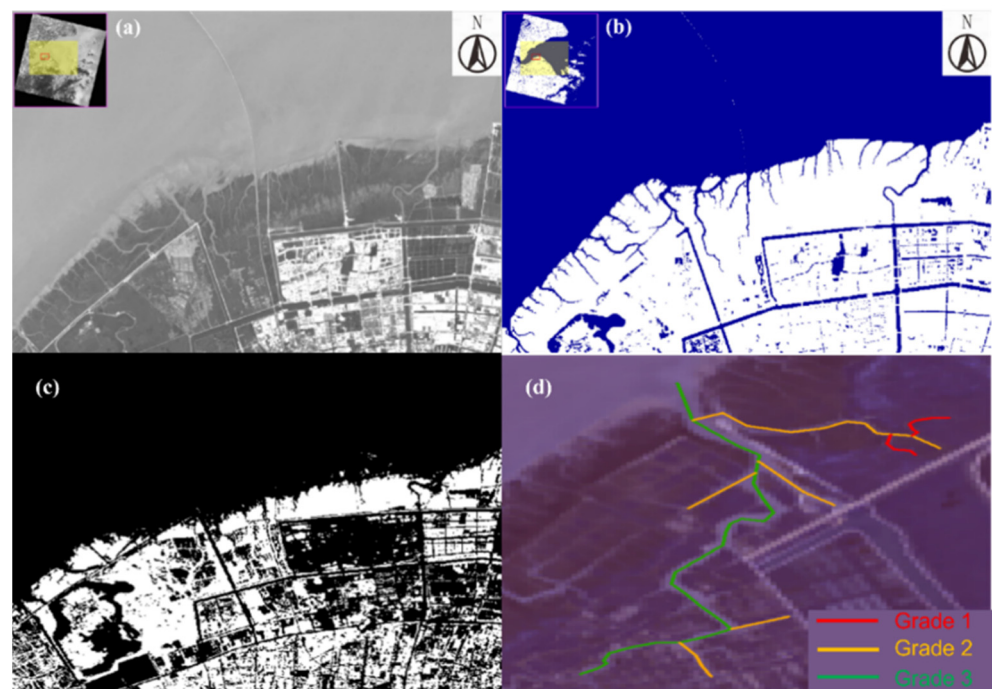
### 2.2.4. Vegetation

Vegetation area calculation in tidal flat areas mainly uses different vegetation index methods, such as the normalized vegetation index (*NDVI*), land surface water index (*LSWI*), and enhanced vegetation index (*EVI*) [62]. In this study, *NDVI* methods were used to extract vegetation because they can distinguish the vegetation area on the tidal flat [63].

$$NDVI = \frac{\rho_{NIR} - \rho_{RED}}{\rho_{NIR} + \rho_{RED}} \qquad (7)$$

where $\rho_{NIR}$ and $\rho_{RED}$ are the reflectances of the remote sensing images in the near-infrared and infrared bands, respectively.

$NDVI > 0.2$ was used for the vegetation areas of the tidal flat [63], and the vegetation area was extracted (Figure 4c).



**Figure 4.** (**a**,**b**) Comparison of the contour of the tidal creeks before and after image segmentation; (**c**) vegetation area extracted by NDVI (white area); (**d**) tidal creek classification in study area using the Horton—Strahler grading method [64].

The spatial distribution of tidal flat vegetation is uneven. Natural vegetation gradually develops from an uneven to regular distribution on a bare tidal flat and eventually dies over time [65]. Therefore, the spatial distribution pattern of the vegetation community is characterized by the development and stage of tidal flat vegetation.

The cohesion index reflects the connection of the natural landscape—that is, the aggregation and dispersion of patches within the landscape. Here, we used the cohesion index to represent the vegetation distribution:

$$COHESION = \left[1 - \frac{\sum_{j=1}^{m} p_{ij}}{\sum_{j=1}^{m} p_{ij} \sqrt{a_{ij}}}\right] \left[1 - \frac{1}{\sqrt{A}}\right]^{-1} \times 100 \tag{8}$$

where $p_{ij}$ represents the perimeter of the jth patch in the ith landscape (unit: m), $a_{ij}$ represents the area of the jth patch in the ith landscape (unit: m$^2$), and $A$ is the total area of the landscape (unit: hm$^2$). The cohesion index ranges between $-1$ and $1$. When the value is $-1$, the vegetation distribution is scattered. When the value is $0$, the vegetation distribution is random. When the value is $1$, the vegetation distribution is aggregated.

### 2.2.5. Tidal Creek

Remote sensing-based tidal flat extraction methods are mainly divided into two types. The first involves the manual delineation of the tidal creek contour using visual interpretation. The second involves semi-automatic extraction of the tidal creek using various algorithms, considering the data quality and extraction efficiency [66].

The pixel gray value of the tidal creeks is distinct from that of the surrounding objects. We used the bias-corrected fuzzy clustering method (BCFCM) to better distinguish the tidal creeks [67]. The image-enhancement method based on the Hessian matrix was used to clarify the edge of the tidal creeks, and the OTSU threshold segmentation method was then used to extract tidal creeks preliminarily [68].

The images of the tidal creeks processed by the algorithm were compared with the original images and manually adjusted using a visual interpretation method to complete the extraction of the tidal creeks. Then, the number, total length, and density of the tidal creeks, as well as their spatial distribution and development characteristics, were characterized using the following methods and parameters:

(1) Tidal creek classification. The Horton–Strahler grading method [64,69] was used to classify tidal creeks. The tidal creek extending directly to the origin of the tidal creek (landward end) was classified as grade 1. There is no bifurcation in the grade 1 tidal trench; two or more grade 1 tidal creeks merge into grade 2, numbered successively until the entire tidal creek system is covered. If two tidal creeks of different grades merge simultaneously, the higher-grade tidal creek is counted (Figure 4d) [70].

(2) Curvature of the tidal creek. The tidal creek curvature was used to represent the curvature of the tidal creek, and its value was equal to the ratio of the total length of the tidal creek to the straight-line distance from the origin of the tidal creek to the point of entry into the sea. The greater the curvature of the tidal creek, the higher the curvature of the tidal creek.

(3) Bifurcation rate of the tidal creek. The bifurcation rate of the tidal creek is an important index used to characterize the development of the tidal creek system, and its value is equal to the number of tidal creek intersection points in one unit of the tidal flat area [24]. The higher the bifurcation rate, the more mature the tidal creek system.

(4) Swing rate of the tidal creek. The tidal creek swing rate was used to quantitatively characterize the stability and spatial variation of the tidal creek system. Its value is the average annual horizontal swing distance of the tidal creek (m/y) [71].

## 3. Results

### 3.1. Elevation

Sixty-five Sentinel-2 images in the study area with cloud percentages lower than 10% were collected. These images can be classified into two types (Figure 5a(I,II)). The images were used to calculate the NDVI (Equation (8)) to recognize waterlines. Then, the number of inundations for each pixel was counted to obtain the inundation frequency *inunfre* (Equation (1)) (Figure 5c,d); $f(obsh, inunfre)$ is a linear function: $y = 10.3783x + 10.8347$ (Figure 5b). Then, the tidal flat elevation was obtained (Figure 6a,b). The gray and the red frames indicate areas being reclaimed or influenced by human activities. Blue represents the area of the sea that is always covered by water, and yellow indicates areas that are covered by vegetation. Thus, the elevation of the area between the blue and yellow can be accurately estimated.

The tidal flat elevation in the areas shown in Figure 6c was obtained by field observation. The retrieved elevation data reproduced the field observation data (Figure 6c,d). The measured elevation of the points at the selected path (red line in Figure 6c,d) correlated highly with the inundation frequency, with a correlation coefficient of 0.73. The large discrepancy in the blue box (Figure 6e,f) is due to a long submersion time.

The elevation in the tidal flat ranges from 10 to 18 m. The higher elevation occurs in the middle of the Andong section, and the lower elevation occurs west of the Andong section, where there are several main tidal creeks.

### 3.2. Area

The offshore boundary of the southern tidal flat in the HZB was a relatively smooth arc in 2020. The land boundary showed an obvious regular shape affected by artificial seawalls and structures. Excluding the TP reclamation project, the tidal flat was wide in the middle and narrow on both sides (Figure 3c). Near the HZB Bridge (bold blue line), the maximum width of the tidal flat reached 9.78 km in the middle part (Andong), while the width of the tidal flat was only 1.42 km on the narrow eastern side (Zhenhai).
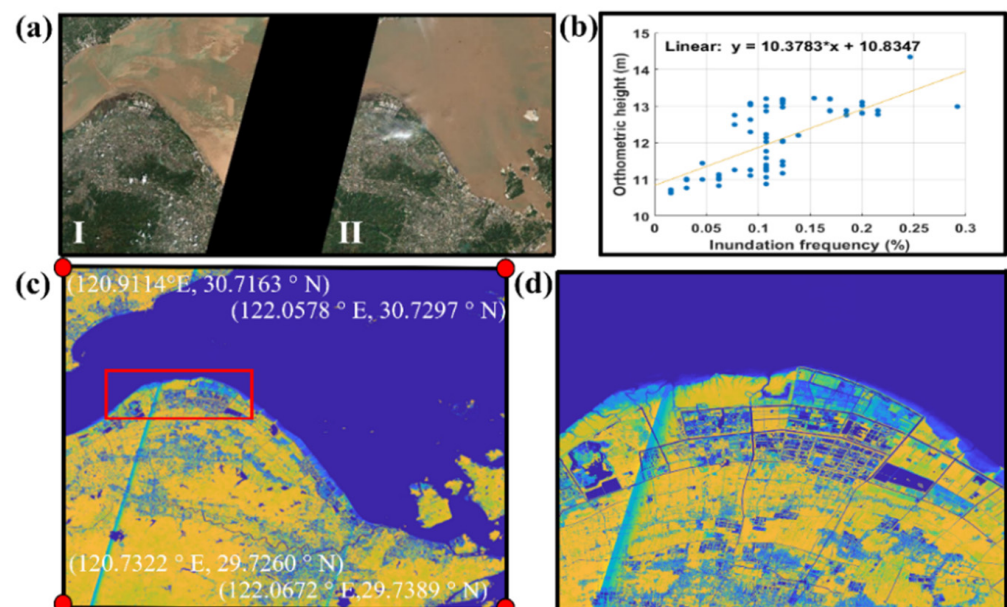


**Figure 5.** (**a**) Two types of Sentinel-2 images; (**b**) the relationship between height and inundation frequency; (**c**) the inundation frequency in HZB, the red dots represent the positions of the four latitude and longitude coordinates in the image, the different colors represent the inundation frequency that blue tends to drown, yellow tends to expose; (**d**) the enlargement of the red frame in (**c**).
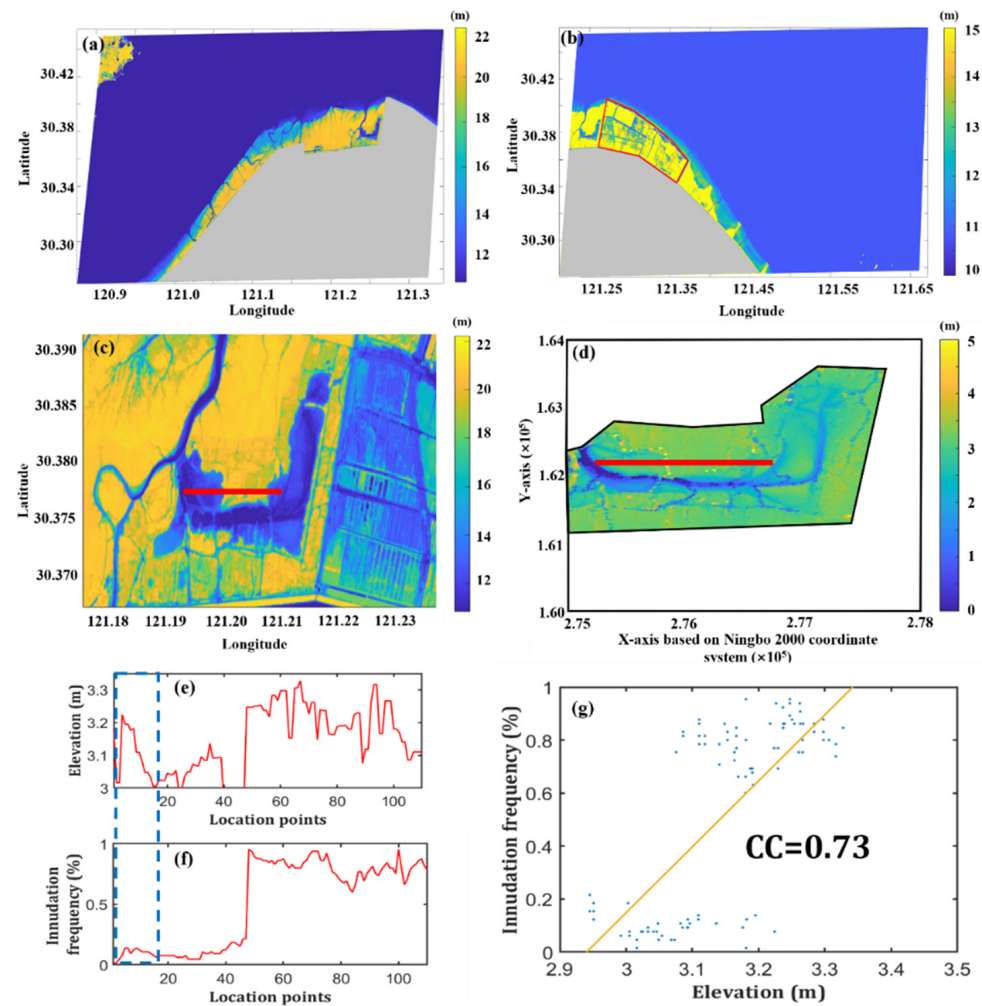
**Figure 6.** (**a,b**) Tidal flat elevation calculated using remote sensing data, red box is the TP reclamation project; (**c**) tidal flat elevation for validation; (**d**) observation data area; (**e,f**) observed elevation data and the calculated inundation frequency at the red line shown in (**c,d**), blue box is the range with large difference; (**g**) the correlation analysis.

In the past 30 years (1990–2020), the total area of the southern tidal flat decreased continuously (Figure 7a), from 749.27 km² to 281.49 km², with a total reduction of 467.78 km², which was 16.2% of the total tidal flat areas in Zhejiang Province in 2010. On the western side of the tidal flat, nearly 121.38 km² of the tidal flat was reclaimed, and 115.28 km² of sandbanks disappeared (Figure 7b). The largest decrease occurred in the middle section of the tidal flat, largely due to large-scale reclamation activities. Human activities led to a continuous advancement in the coastline toward the sea and the gradual transformation of the coastline from a naturally smooth shape to an artificial coastline (Figure 7c). Comparing the coastlines in the Andong section between 1990 and 2020, the largest distance of the coastline moving seaward was 9.19 km, and the shortest distance was 2.06 km. The area decreased by 51.7% from 390.24 km² to 188.45 km². The shape of the tidal flat changed from left-convex to convex. The sharp reduction in the tidal flat area from 2005 to 2010 is also due to the tidal flat reclamation over these five years. The average distance of the coastline moving seaward was more than 2.60 km.
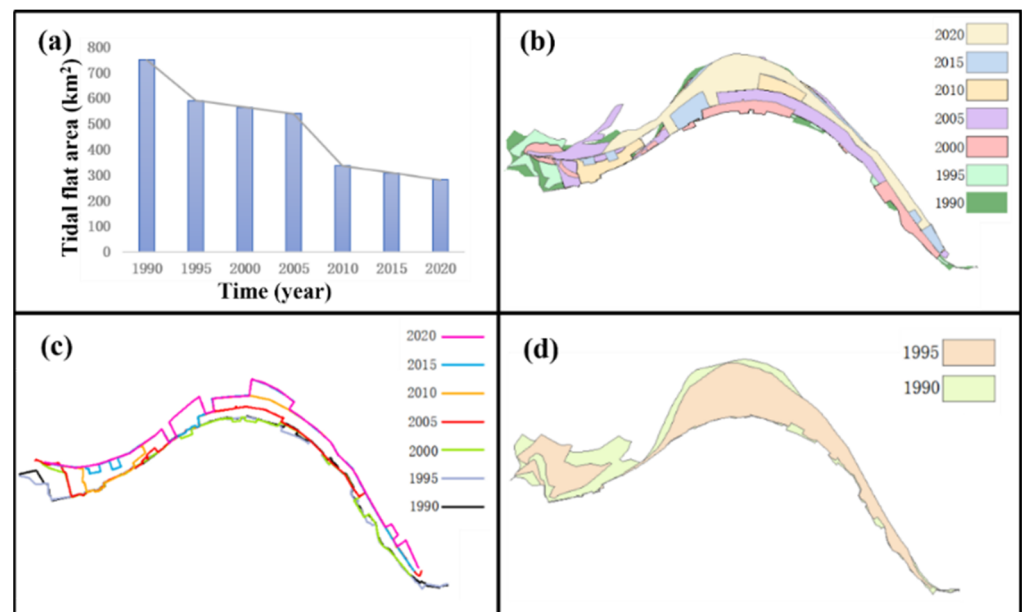
**Figure 7.** Southern tidal flat of HZB from 1990 to 2020. (**a**) Changes in tidal flat area; (**b**) regional changes in tidal flat; (**c**) artificial coast; (**d**) comparison between 1990 and 1995 tidal flats.

### 3.3. Slope

The topography of the tidal flat from the Yuyao section to the western part of the Andong section can be categorized as an erosive convex profile. In contrast, the Cixi section can be categorized as an erosive concave profile. The average slope of each section was relatively small (Table 2). During 1990–2020, except for a few sections, the average slope of all the sections was <1. The slopes of sections 8# and 36# changed the most during the past 30 years, and there was a reciprocal transformation of the positive slope and the reverse slope. The slopes of the other sections remained stable (Table 3).

**Table 2.** Tidal levels, horizontal projection distances, and average slopes of sections in 2020.

| Section | 8# | 14# | 19# | 24# | 28# | 36# | Date |
|---|---|---|---|---|---|---|---|
| Tidal level (m) | −0.77 | −0.03 | 0.62 | 0.78 | 0.52 | 0.27 | 28 March 2021 (Low water level) |
| | −0.22 | −0.23 | −0.19 | −0.13 | −0.12 | −0.11 | 16 August 2020 (Medium water level) |
| | −1.12 | −0.55 | 0.15 | 0.11 | 0.11 | 0.17 | 12 May 2020 (High water level) |
| Horizontal projection distance (km) | 0.34 | 0.16 | 2.05 | 0 | 1.19 | 0 | 28 March 2021 (Low water level) |
| | 0.84 | 1.81 | 3.11 | 0.01 | 1.46 | 0.87 | 16 August 2020 (Medium water level) |
| | 1.72 | 2.83 | 8.68 | 2.11 | 2.72 | 1.53 | 12 May 2020 (High water level) |
| Average slope | 0.24 | 0.2 | 0.1 | 0.43 | 0.703 | 0.07 | |

**Table 3.** Average slope of each section on the southern bank of HZB.

| Section | 8# | 14# | 19# | 24# | 28# | 36# | Time (Year) |
|---|---|---|---|---|---|---|---|
| Average slope | −1.07 | 0.33 | 1.48 | 0.99 | 0.79 | −0.78 | 1990 |
| | 1.71 | 0.32 | 0.238 | 0.16 | 0.589 | 2.61 | 1995 |
| | 1.47 | 0.29 | 0.24 | 0.27 | 0.25 | 0.05 | 2000 |
| | −1.45 | 0.327 | 0.25 | 0.27 | 0.95 | −0.02 | 2005 |
| | 1.21 | 0.527 | 0.36 | 0.58 | 0.95 | 2.07 | 2010 |
| | −1.53 | 0.27 | 0.42 | 0.20 | 0.89 | 0.36 | 2015 |
| | 0.24 | 0.2 | 0.1 | 0.43 | 0.7 | 0.07 | 2020 |

In Section 8#, there was an erosional concave profile (1990, 2000, 2015), an erosional convex profile (2005, 2010, 2020), and a gentle slope profile (1995). The sharp slope changes

from 1990 to 1995 were caused by the disappearance of the sandbar in the Yuyao section. However, the large slope changes from 2005 to 2010 were caused by the steep slope produced by the artificial coastline advancement seaward after reclamation. Section 36 is located in the tidal flat of the Cixi section, which is relatively narrow. The advancement of the artificial coastline seaward after reclamation led to large terrain changes near the land and influenced the average slopes.

The artificial coastline also impacted Sections 14#–28#. Section 24# is affected by the TP seawall. The waterlines coincided with the seawall for an extended time (Figure 8c), which reflects the existence of an artificial seawall. However, the larger widths of these sections weakened the effect on the slopes. For example, after the embankment construction due to the TP reclamation project in Section 24# in 2010–2015, the tidal flat slope changed slightly.
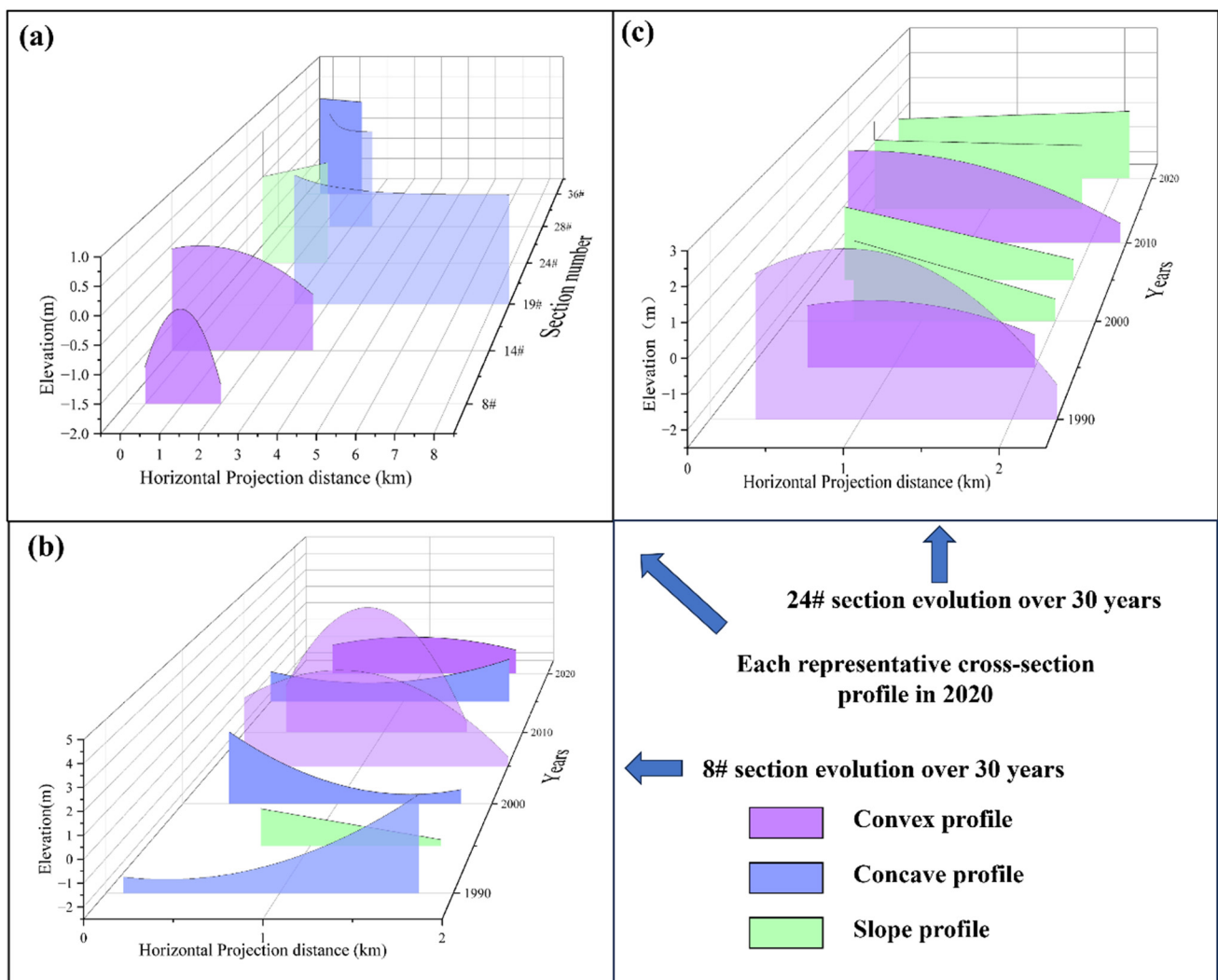


**Figure 8.** (**a**–**c**) Topography fitting curves of the cross-sections.

### 3.4. Vegetation

Over the past 30 years, vegetation has mainly concentrated in the supratidal zone of the tidal flat, and most vegetation has grown close to the coastline. The interannual vegetation change in this region presented a certain periodicity, with two turning points appearing in 2000 and 2020 (Figure 9c). Before 2000, both the vegetation area and proportion of vegetation showed a decreasing trend, and the turning point appeared in 2000, reaching the first peak. At this time, the vegetation area reached 64.98 km$^2$, and the proportion of vegetation reached 11.5%. During 2000–2005, there was a sharp decline in the vegetation

area, and it continued to decline in subsequent years. As the tidal flat area decreased from 2005 to 2015, the proportion of vegetation increased.
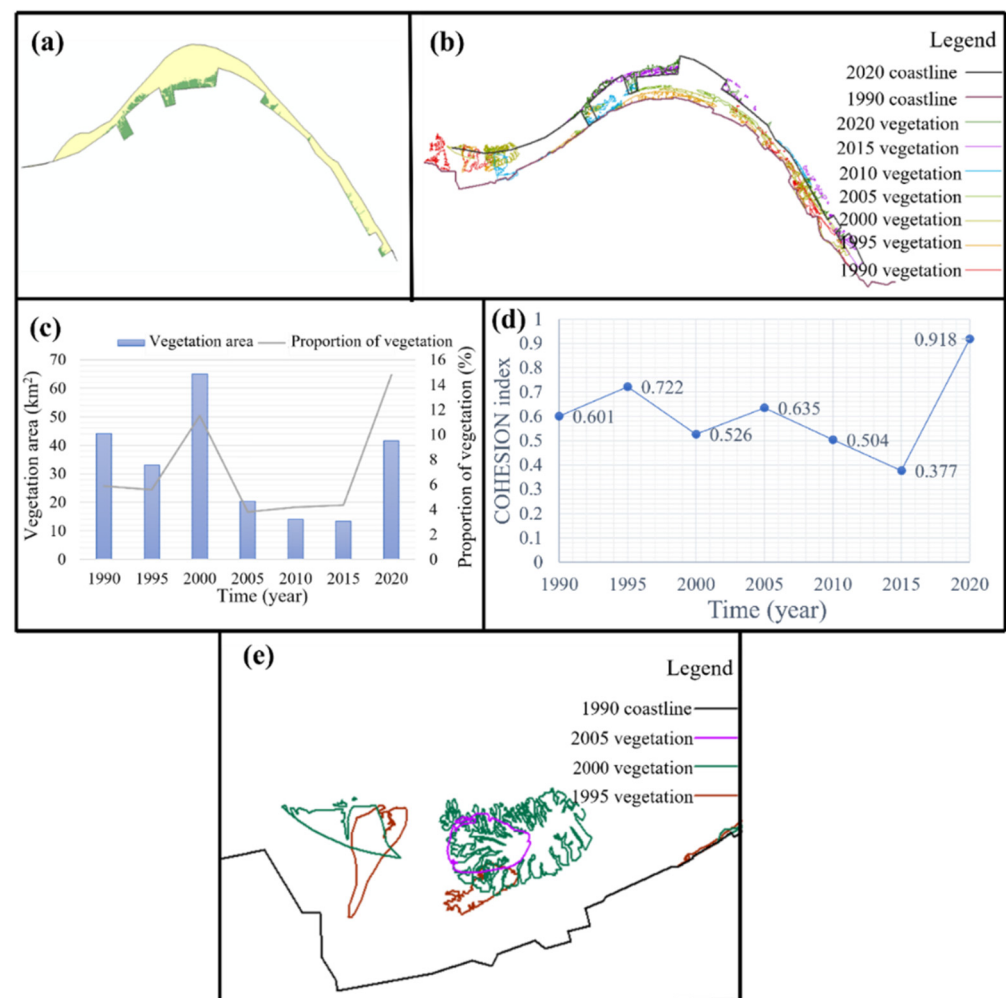


**Figure 9.** (**a**) Spatial distribution of tidal flat vegetation on the south bank of HZB; (**b**) changes in tidal flat vegetation in the south bank of HZB during 1990–2020; (**c**) statistics of tidal flat vegetation change in the south bank of HZB; (**d**) cohesion index of tidal flat vegetation in the south bank of HZB from 1990 to 2020. (**e**) changes in tidal flat vegetation in Yuyao Section from 1995 to 2005.

The increase in the vegetation area and proportion before 2000 and the sharp decline after 2000 were due to the changes in the vegetation area on the sandbank of the Yuyao section from 1995 to 2005. A radially vast vegetation community developed in the tidal flat (where the altimetry was high), with a short evolution process of "grow–mature–degrade" (Figure 9e). The area and proportion of vegetation reached a second peak in 2020. Before 2015, the artificial coastline was completely established. Outside the artificial coastline of the reclamation seawall, vegetation began to develop from patchy to aggregated, forming a large-scale salt marsh with a vegetation area of 41.62 km$^2$. The vegetation was mainly distributed in the U-shaped artificial seawall near the Andong section, which showed a large area of banded distribution. In the Zhenhai section, scattered patches of vegetation were largely attached to the vicinity of the dike. During this period, the cohesion index of the tidal flats increased from 0.38 in 2015 to 0.92 in 2020. This indicates that tidal flat vegetation developed into a new mature stage in 2020. Simultaneously, the tidal flat area was further reduced, resulting in a tidal flat vegetation ratio reaching a 30-year high of 14.8%. During 2010–2015, after the outer seawall was built, a bare tidal flat formed outside the seawall. The landscape pattern of the tidal flat vegetation was different on the east and

west sides of the TP reclamation seawall. The vegetation exhibited low aggregation in the eastern section of Cixi to Zhenhai, with a vegetation cohesion index of 0.12.

### 3.5. Tidal Creeks

In 2020, the total length and the density of the tidal creeks were 105.83 km and 0.38 km/km$^2$ on the southern tidal flat of HZB, respectively. Compared with typical tidal flats in China [20–70,72], the tidal creek density was low, mainly because of the heterogeneous spatial distribution. All tidal creeks were distributed in the tidal flat from Yuyao to the Andong section, forming a complex tidal creek system. There were no tidal creeks between the Cixi and Zhenhai sections. The curvature of the tidal creek was 1.11, and the branching rate was 0.24. Among them, middle- and low-grade (grade 1 and grade 2) tidal creeks accounted for a relatively high proportion of 91.4%. The highest grade was grade 4, indicating that the tidal creek network passed the primary stage of development (Table 4).

**Table 4.** Tidal creek parameters.

| Year | Number | The Ratios of Each Grade (%) | | | | Parameters | | | |
|------|--------|---------|---------|---------|---------|-------------|--------------------|-----------|--------------------------------|
| | | Grade 1 | Grade 2 | Grade 3 | Grade 4 | Length (km) | Density (km/km$^2$) | Curvature | Branching Rate (per km$^2$) |
| 1990 | 51 | 0.75 | 0.2 | 0.06 | 0 | 112.54 | 0.15 | 1.01 | 0.03 |
| 1995 | 41 | 0.83 | 0.17 | 0 | 0 | 73.89 | 0.13 | 1.03 | 0.03 |
| 2000 | 64 | 0.84 | 0.14 | 0 | 0 | 96.19 | 0.17 | 1.070 | 0.04 |
| 2005 | 21 | 0.86 | 0.14 | 0 | 0 | 45.95 | 0.09 | 1.04 | 0.01 |
| 2010 | 26 | 0.85 | 0.15 | 0 | 0 | 81.46 | 0.24 | 1.15 | 0.03 |
| 2015 | 77 | 0.70 | 0.2 | 0.08 | 0.03 | 105.93 | 0.34 | 1.07 | 0.19 |
| 2020 | 117 | 0.74 | 0.18 | 0.06 | 0.03 | 105.83 | 0.38 | 1.11 | 0.24 |

The development of tidal creeks on the southern tidal flat of HZB took place in three stages (Table 4). The first is the primary stage from 1990 to 2005, the second is the mature stage from 2005 to 2015, and the third is the regeneration stage from 2015 to 2020. The last five years of the second stage (2010–2015) are regarded as the transitional stage from maturity to redevelopment.

During the primary stage (1990–2005), the tidal flat topography changed frequently, especially in the Yuyao section. Tidal creeks were mostly unstable, with frequent formation and extinction, because the intertidal zone was mostly categorized as a silty gentle slope or a shallow erosion zone (Figure 10). The tidal creeks were immature, low in number, and mostly low-grade. The curvature ranged from 1.01 to 1.07, meaning the tidal creeks mostly developed in a straight line and extended longitudinally. The branching rate of the tidal creeks was low (<0.05), and the tidal creeks were relatively independent.

Prior to 2005, the total length of the tidal creeks irregularly varied. As the tidal flat area was wide, the density of the tidal creeks was low. Beginning in 2005, the tidal creek network developed rapidly, with the total length and density increasing annually. During the mature stage (2005–2015), tidal flat erosion and silting tended to be stable. The total length of the tidal creeks increased continuously, and the tidal creek density increased annually due to the decrease in the tidal flat area. The tidal creeks developed from immature to mature, with an increase in grade and total number of tidal creeks. The branching rate increased annually, and finally, a complex network was formed in 2015. The TP reclamation project was built in 2010, and a large bare tidal flat outside the seawall was formed. The tidal creeks became more erodible due to vegetation loss [28,73,74]. A large area characterized by tidal creeks disappeared. The tidal creek network gradually developed, forming a mature tidal creek system inside the U-shaped seawall.
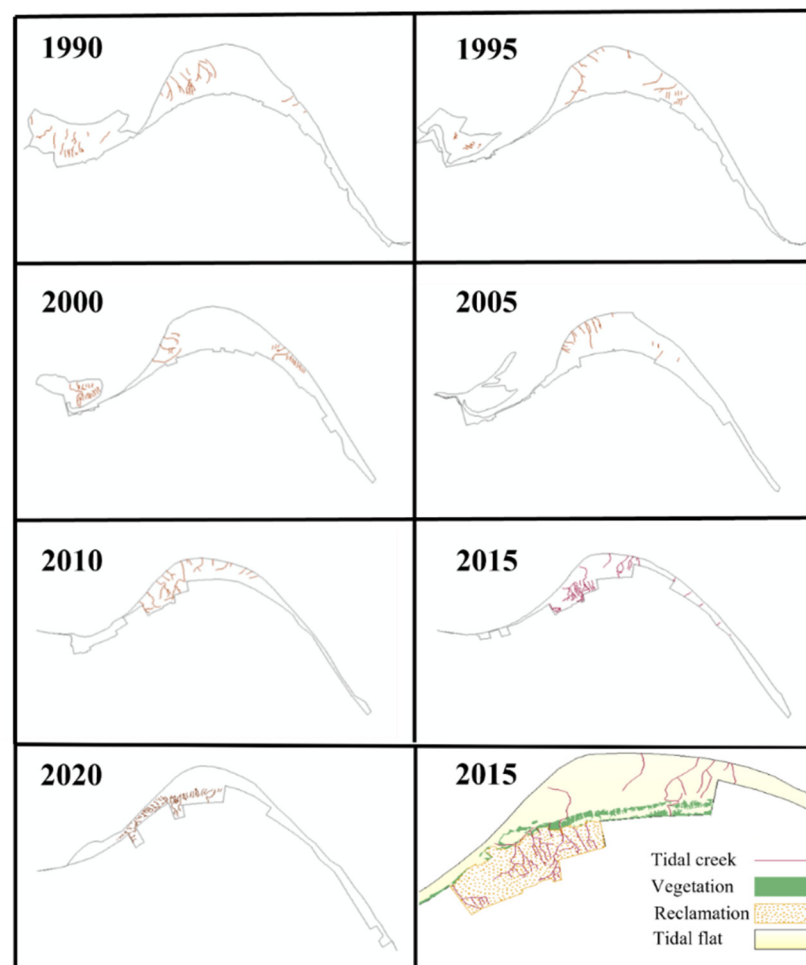
**Figure 10.** Tidal creek distribution of tidal flat on the south bank of HZB 1990–2020 and a detailed tidal flat information in 2015.

During the regeneration stage (from 2015 to 2020), the seawall expanded in the 2015 reclamation area, damaging the original tidal creek network. Except for a few high-grade tidal creeks, middle- and low-grade tidal creeks disappeared. Tidal creeks were redeveloped, and a new system was formed. By 2020, many radial tidal creeks surrounding the artificial seawall had formed in the Yuyao and Andong sections.

Tidal creeks were mainly developed in tidal flats with gentle slopes and large areas and widths, such as the radial sandbar in the Yuyao section and the intertidal zone in the Andong and Cixi sections. There were a few tidal creeks in the Zhenhai section, which had a small width and uniform slope.

## 4. Discussion

### 4.1. Impacts of Human Activity on Tidal Flat

Human activities are closely related to the tidal flat morphology in this area, including the HZB Bridge, dike, and reclamation. Reclamation has been the most active human activity in this tidal flat over the last 30 years. The reclaimed area each year was mainly near the shoreline in the Andong section. Reclamation is often accompanied by seawall construction, which directly affects the changes in morphology in the tidal flat area.

Firstly, the artificial coastline directly reduced the tidal flat area. The large change in the artificial coastline of the Cixi to Zhenhai section was the main reason for the variation in the tidal flat area. The correlation between the tidal flat area and artificial coastline advancement is $R^2 = 0.89$ (Figure 11b). The continuous reclamation and artificial coastline led to a reduction in the tidal flat area. Reclamation activities on the southern bank of HZB

occurred from 2000 to 2015 and began to decrease after 2015. This led to a changing rate of decrease in the tidal flat area. Secondly, artificial seawalls altered tidal flat morphology. For example, after the seawall was built in the TP reclamation area in 2010, tidal flat vegetation outside the seawall quickly disappeared (Figure 9b), and the tidal creek degraded (Figure 10). Finally, the tidal flat changed from a complex natural habitat to a bare flat with a gentle slope.
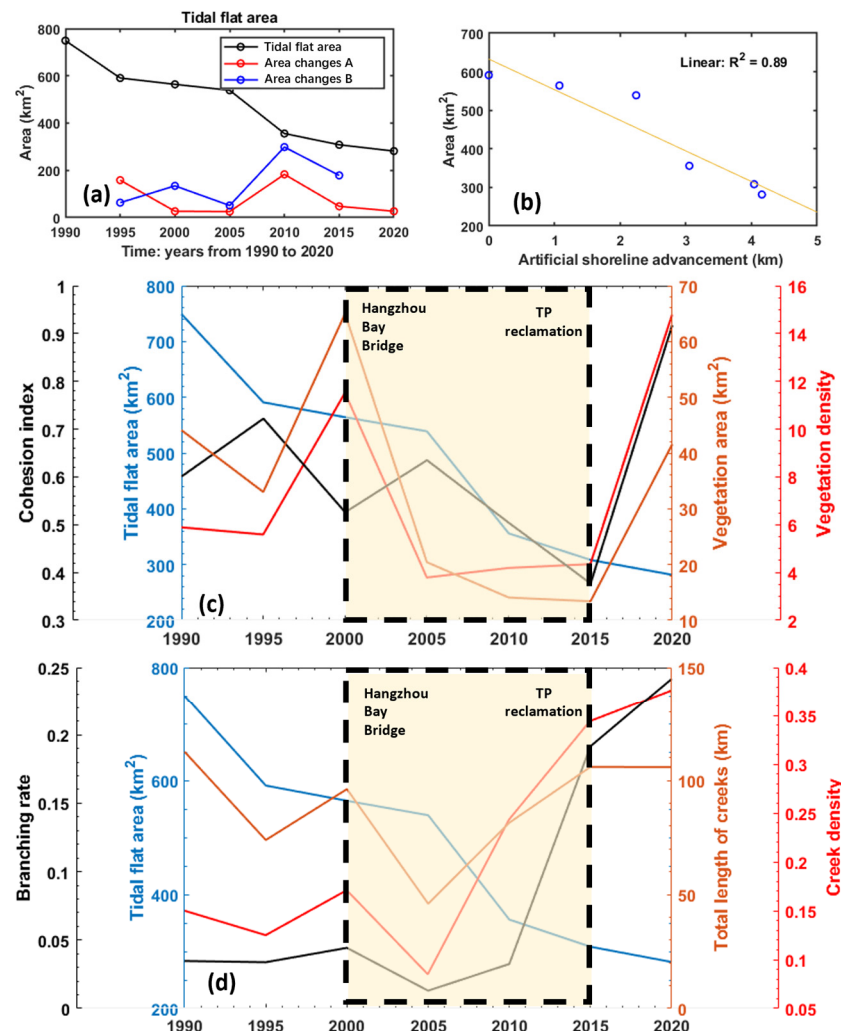


**Figure 11.** (**a**) Tidal flat area: black line represents the tidal flat area in this study, blue line represents the changes in tidal flat in this study, and red line represents the changes in tidal flat we calculated with the tidal flat area data in Ye et al. [75]; (**b**) correlation analysis of tidal flat area and human activity; (**c**) tidal flat area and vegetation information; (**d**) tidal flat area and creek information; black dotted frame with yellow background represents the period of great human activities: mainly reclamation and artificial coastline advancement. HZB Bridge was built from 2000 to 2005; TP reclamation was built from 2010 to 2015.

The HZB Bridge was built in 2003. The shape of the tidal flat was left-skewed before 2005 and then became normal (Figure 10). The bridge was built west of the tidal flat (Figure 12a). A trailing vortex area of more than 1 km was formed behind the pile foundation, and high velocity was formed between the pile foundations [76]. This condition might impact the tidal flat [77]. After the bridge's construction, the southward sediment fluxes at the east side of the bridge were enhanced, contributing to tidal flat evolution [76]. The dikes were mainly constructed in the Zhenhai section. As the dikes weakened the hydrodynamics and promoted siltation, deposition appeared near the dike [78] (Figure 12b).
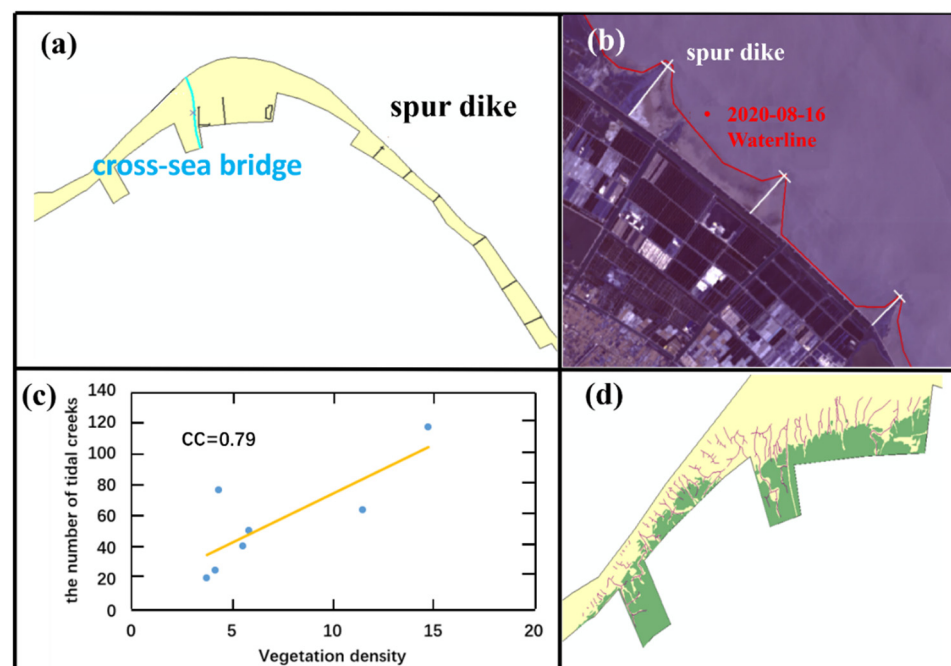
**Figure 12.** (**a**) Distribution of coastal structures; (**b**) deposition near the spur dikes; (**c**) the correlation between vegetation density and the number of tidal creeks; (**d**) tidal creek network on the west tidal flat of Andong section in 2020, green area is vegetation, yellow area is tidal flat and purple lines are tidal creeks.

The completion of the Three Gorges Dam has caused a sharp decrease in sediment loads in the upper reaches of the Yangtze River since 2003 [79,80]. Middle and lower river channels change from sediment sinks to sediment sources [34]. The decrease in sediment loads from the Changjiang River changed the seabed from deposition to erosion in the northern part of Hangzhou Bay's mouth. The overall effect of the decreased sediment loads from the Changjiang River estuary (CRE) on Hangzhou Bay was not obvious, and the sediment deposition rate even increased after 2003 [81].

Human activities play a major role in vegetation and tidal creeks. During 1990–1995 and 2000–2005, the tidal flat area decreased, as did vegetation and tidal creeks. Vegetation is usually located near the shoreline, making it more susceptible to reclamation. The tidal creeks extend from the vegetation to the sea (Figure 12c). During 2005–2010, tidal creeks recovered significantly, but vegetation did not because the tidal creeks away from the vegetation experienced minor impacts from reclamation. Both vegetation and tidal creeks are affected by tidal flat areas, and the tidal creek and tidal flat area exhibit a negative correlation. The correlation coefficient (CC) relating the tidal flat area and creek density/curvature/branching rate is −0.93, −0.79, and −0.73, respectively.

### 4.2. Correlation between Vegetation and Tidal Creek

Complex interaction exists between tidal creeks and vegetation [21,23]. A tidal creek may lead to vegetation development [82], and vegetation may also promote or inhibit the development of a tidal creek [15,17]. Owing to the clustered distribution of vegetation in this region, the underlying surface roughness of the region is increased [64], so that more water must be discharged at a low tide. As a result, the tidal creeks in this region are dense, and most of the water enters the tidal flat vegetation area, forming a rich catchment network [15]. The number of tidal creeks increased with the increase in vegetation density, and the CC value was 0.79 (Figure 12c). Furthermore, because vegetation constrained the lateral swing and development of tidal creeks [28], tidal creeks inside the vegetation area are mostly high-grade, which are longer in the longitudinal direction and have fewer branching points (Figure 12d).

*4.3. Uncertainty Analysis*

In tidal flat area estimation, remote sensing images and tidal levels of TPXO were combined to determine the upper and lower boundaries of the tidal flats. However, some uncertainties exist, including data source and processing errors [83]. Firstly, the satellite image resolution is $10 \times 10$ m, resulting in a possible pixel error of $1 \times 10^{-4}$ km$^2$. The study area (>280 km$^2$) is sufficiently large to effectively reduce the pixel error. Therefore, it is reasonable for us to keep the length and area data to two decimal places in the paper. Secondly, tidal levels of TPXO were used to replace the elevation of upper and lower boundaries. The accuracy of the TPXO data, the number of profiles, and the satellite image accurately capturing the upper and lower boundaries all affect the area estimation.

In tidal flat elevation estimation, the estimation method has limitations; only the elevation of frequently exposed and submerged areas can be estimated accurately. The large difference in the data shown in the blue box (Figure 6e,f) also indicates that the method has disadvantages for long-time submerged regions. The effectiveness of the estimates also depends on vegetation, the number of images or the time span of all the images, and the availability of satellite or measured elevation data for the corresponding time.

**5. Conclusions**

The tidal flat in Hangzhou Bay plays an important role in coastal engineering and estuarine hydrodynamics. Using remote sensing data, we investigated the variations in tidal flat topography, vegetation, and tidal creeks over the past 30 years, from 1990 to 2020. The overall elevation of the tidal flat was calculated using remote sensing data combined with RTK data collected in the field, and the result clearly identifies the tidal creeks and vegetation present on the tidal flat.

High-quality elevation data for the southern tidal flat in HZB were retrieved using this method and validated with a CC value of 0.73. The results show that the elevation in the tidal flat ranges from 10 to 18 m. Higher elevations are found in the middle of the Andong section, and lower elevations occur in the western Andong section. From 1990 to 2020, the total area of the tidal flat decreased from 749.27 to 281.49 km$^2$, with a total reduction of 467.78 km$^2$. The average slope of the tidal flat was less than 0.8, with erosive concave/convex profiles. The tidal flat slope is relatively small in general, and the slope of the tidal flat varies at different locations, indicating that the sediment deposition rate differs.

Vegetation is mainly located in the supratidal zone and grows near the shoreline. The vegetation area generally decreased, with two turning points in 2000 and 2020. A bare tidal flat appeared outside the TP seawall after 2010. The tidal creek network was divided into three stages from 1990 to 2020: the primary stage, the mature stage, and the redevelopment stage. In 2020, middle- and low-grade tidal creeks accounted for a high proportion of all tidal creeks (91.4%) with a curvature of slightly >1. The total length and branching rate of tidal creeks, respectively, decreased from 112.54 km and 0.03 per km$^2$ to 45.95 km and 0.01 per km$^2$, and then reached a minimum in 2005 before returning to 105.83 km and 0.24 per km$^2$ in 2020.

Artificial coastlines related to reclamation are the main reason for the decrease in the tidal flat area. The number of tidal creeks increased with the increase in vegetation density. Additionally, tidal creeks well within the vegetation area were mostly high-grade, longer, and had fewer branches.

**Author Contributions:** Conceptualization, L.L.; Methodology, L.L., F.S., Y.X., H.S. and Z.H.; Validation, F.S.; Investigation, F.S.; Data curation, F.S.; Writing—original draft, L.L. and F.S.; Writing—review & editing, L.L., Y.X., H.S., N.W., Z.H. and K.G.; Visualization, F.S.; Funding acquisition, L.L., Y.X., N.W. and Z.H. All authors have read and agreed to the published version of the manuscript.

## References

1.   Zhang, C.; Gong, Z.; Chen, Y.; Tao, J.; Kang, Y.; Zhou, J.; Zhou, Z. Research progress and frontier problems of tidal flat evolution. In Proceedings of the 18th China Symposium on Ocean (Shore) Engineering, Zhoushan, China, 23–25 September 2017.
2.   Gong, Z.; Huang, S.; Xu, B.; Zhu, S.; Zhang, Y.; Zhou, Z. Evolution of tidal flat in response to storm surges: A case study from the central Jiangsu Coast. *Adv. Water Sci.* **2019**, *30*, 243–254.
3.   Gong, Z.; Zhang, Y.; Zhao, F.; Zhou, Z.; Zhang, C. Advances in coastal storm impacts on morphological evolution of mud tidal flat-creek system. *Adv. Sci. Technol. Water Resour.* **2019**, *39*, 75–84.
4.   Hu, C.; Pan, C.; Wu, X.; Tang, Z.; Zheng, J. Tidal flat evolution law and its mechanism on the south bank of Hangzhou Bay from 1959 to 2019. *Adv. Water Sci.* **2021**, *32*, 230–241.
5.   Yang, Y.; Wang, Y.; Gao, S.; Wang, X.; Shi, S.; Zhou, L.; Li, G. Sediment resuspension in tidally dominated coastal environments: New insights into the threshold for initial movement. *Ocean. Dyn.* **2016**, *66*, 401–417. [CrossRef]
6.   Zhang, X.; Chen, Y.; Le, Y.; Zhang, D.; Yan, Q.; Dong, Y.; Han, W.; Wang, L. Nearshore bathymetry based on ICESat-2 and multispectral images: Comparison between Sentinel-2, Landsat-8, and Testing Gaofen-2. *IEEE J. Sel. Top. Appl. Earth Obs. Remote Sens.* **2022**, *15*, 2449–2462. [CrossRef]
7.   Hsu, H.; Haung, C.; Jasinski, M.; Li, Y.; Gao, H.; Yamanokuchi, T.; Wang, C.; Chang, T.; Ren, H.; Kuo, C.; et al. A semi-empirical scheme for bathymetric mapping in shallow water by ICESat-2 and Sentinel-2: A case study in the South China Sea. *J. Photogramm. Remote Sens.* **2021**, *178*, 1–19. [CrossRef]
8.   Xu, N.; Ma, Y.; Yang, J.; Wang, X.; Wang, Y.; Xu, R. Deriving tidal flat topography using ICESat-2 laser altimetry and Sentinel-2 imagery. *Geophys. Res. Lett.* **2022**, *49*, e2021GL096813. [CrossRef]
9.   Yang, J.; Ma, Y.; Zheng, H.; Xu, N.; Zhu, K.; Wang, X.; Li, S. Derived depths in opaque waters using ICESat-2 photon-counting lidar. *Geophys. Res. Lett.* **2022**, *49*, e2021GL100509. [CrossRef]
10.  Zhang, X.; Lin, P.; Gong, Z.; Li, B.; Chen, X. Wave attenuation by Spartina alterniflora under macro-tidal and storm surge conditions. *Wetlands* **2022**, *40*, 2151–2162. [CrossRef]
11.  Brodie, J.; Roland, C.; Stehn, S.; Smirnova, E. Variability in the expansion of trees and shrubs in boreal Alaska. *Ecology* **2019**, *100*, e02660. [CrossRef]
12.  Marani, M.; Lanzoni, S.; Zandolin, D.; Seminara, G.; Rinaldo, A. Tidal meanders. *Water Resour. Res.* **2002**, *38*, 1225. [CrossRef]
13.  Lao, C.; Xin, P.; Zuo, Y.; Cheng, L. Effect of fractional vegetation cover on the evolution of tidal creeks of the Jiuduansha shoal in Yangtze River Estuary (China) during 1996–2020. *Adv. Water Sci.* **2022**, *33*, 15–26.
14.  Wu, Y.; Wang, Y.; Zhang, Z. Effects of tidal creek morphology on succession of wetland plant communities in the Yellow River Delta. *Ecol. Sci.* **2020**, *39*, 33–41.
15.  Li, J.; Yang, X.; Tong, Y.; Zhang, D.; Shen, Y.; Zhang, R. Influences of Spartina alterniflora invasion on ecosystem services of coastal wetland and its countermeasures. *Mar. Sci. Bull.* **2005**, *24*, 33–38+4.
16.  Liu, J.; Yang, S.; Shi, B.; Luo, X.; Fu, X. Topography and evolution of the tidal trench in the eastern Chongming tidal flat, Changjiang River Estuary. *J. Mar. Sci.* **2012**, *30*, 43–50.
17.  Chen, Y.; He, Z.; Li, B.; Zhao, B. Spatial distribution of tidal creeks and quantitative analysis of its driving factors in Chongming Dongtan, Shanghai. *J. Jilin Univ. (Earth Sci. Ed.)* **2013**, *43*, 212–219.
18.  Liu, L.; Qu, F.; Li, Y.; Yu, J.; Yang, J.; An, C. Correlation between creek tidal distribution and vegetation coverage in the Yellow River Delta coastal wetland. *Chin. J. Ecol.* **2020**, *39*, 1830–1837. [CrossRef]
19.  Li, Y.; Wu, H.; Zhang, S.; Lu, X.; Lu, K. Morphological characteristics and changes of tidal creeks in coastal wetlands of the Yellow River Delta under Spartina alterniflora invasion and continuous expansion. *Wetl. Sci.* **2021**, *19*, 88–97.
20.  Yu, X.; Han, G.; Wang, X.; Zhang, B. Effects of Spartina alterniflora invasion on morphological characteristics of tidal creeks and plant community distribution in the Yellow River Estuary. *Chin. J. Ecol.* **2022**, *41*, 42–49. [CrossRef]
21.  Gong, Z.; Bai, X.; Ji, C.; Zhao, F.; Zhou, Z.; Zhang, C. A numerical model for the cross-shore profile evolution of tidal flats based on vegetation growth and tidal processes. *Adv. Water Sci.* **2018**, *29*, 877–886.
22.  Yang, S.; Shi, Z.; Zhao, S. Influence of tidal marsh plants on dynamic sedimentation process in the Yangtze River Estuary. *Acta Oceanol. Sin.* **2001**, *4*, 75–80.
23.  Zhou, Z.; Chen, L.; Lin, W.; Luo, F.; Chen, X.; Zhang, C. Advances in bio-geomorphology of tidal flat-saltmarsh systems. *Adv. Water Sci.* **2021**, *32*, 470–484.
24.  Mou, K.; Gong, Z.; Qiu, H. Spatiotemporal differentiation and development process of tidal creek network morphological characteristics in Yellow River Delta. *Acta Geogr. Sin.* **2021**, *76*, 2312–2328. [CrossRef]

25. Zhang, C.; Chen, X. Offshore environment changes and countermeasures in response to large-scale tidal flat reclamation. *J. Hohai Univ.* **2015**, *43*, 424–430.

26. Li, J.; Yang, X.; Tong, Y. Progress on environmental effects of tidal flat reclamation. *Prog. Geogr.* **2007**, *26*, 43–51.

27. Chen, L.; Zhou, Z.; Xu, F.; Jiménez, M.; Tao, J.; Zhang, C. Simulating the impacts of land reclamation and de-reclamation on the morphodynamics of tidal networks. *Anthr. Coasts* **2020**, *3*, 30–42. [CrossRef]

28. Lu, B.; Jiang, X. Reclamation impacts on the evolution of the tidal flat at Chongming Eastern Beach in Changjiang estuary. *J. Remote Sens.* **2013**, *17*, 342–349+335–341.

29. Syvitski, J.P.M. Deltas at risk. *Sustain. Sci.* **2008**, *3*, 23–32. [CrossRef]

30. Wei, W.; Dai, Z.; Mei, X.; Gao, S.; Liu, J. Multi-decadal morpho-sedimentary dynamics of the largest Changjiang estuarine marginal shoal: Causes and implications. *Land Degrad. Dev.* **2019**, *30*, 2048–2063. [CrossRef]

31. Dai, Z.; Fagherazzi, S.; Gao, S.; Mei, X.; Ge, Z.; Wei, W. Scaling properties of estuarine beaches. *Mar. Geol.* **2018**, *404*, 130–136. [CrossRef]

32. Yang, G.; Wang, X.; Zhong, Y.; Oliver, T. Modelling study on the sediment dynamics and the formation of the flood-tide delta near Cullendulla Beach in the Batemans Bay, Australia. *Mar. Geol.* **2022**, *452*, 106910. [CrossRef]

33. Guo, L.; Zhu, C.; Xu, F.; Xie, W.; van der Wegen, M.; Townend, I.; Wang, Z.; He, Q. Reclamation of tidal flats within tidal basins alters centennial morphodynamic adaptation to sea-level rise. *J. Geophys. Res.-Earth Surf.* **2022**, *127*, e2021JF006556. [CrossRef]

34. Dai, Z.; Mei, X.; Darby, S.; Lou, Y.; Li, W. Fluvial sediment transfer in the Changjiang (Yangtze) river-estuary depositional system. *J. Hydrol.* **2018**, *566*, 719–734. [CrossRef]

35. Yuan, R.; Zhang, H.; Qiu, C.; Wang, Y.; Guo, X.; Wang, Y.; Chen, S. Mapping morphodynamic variabilities of a meso-tidal flat in Shanghai based on satellite-derived data. *Remote Sens.* **2022**, *14*, 4123. [CrossRef]

36. Zheng, G.; Wang, Y.; Zhao, C.; Dai, W.; Kattel, G.; Zhou, D. Quantitative analysis of tidal creek evolution and vegetation variation in silting muddy flats on the Yellow sea. *Remote Sens.* **2023**, *15*, 5107. [CrossRef]

37. Han, Q. *Research on the Status of Tidal Resources in China Using Remote Sensing Technology*; Nanjing Normal University: Nanjing, China, 2011.

38. Ye, T. *The Multi-Scale Variations of Suspended Sediment Dynamics in Hangzhou Bay and Its Interaction with Tidal Flat Variations*; Zhejiang University: Zhejiang, China, 2019.

39. Hu, Y.; Yu, Z.; Zhou, B.; Li, Y.; Yin, S.; He, X.; Peng, X.; Shum, C. Tidal-driven variation of suspended sediment in Hangzhou Bay based on GOCI data. *Int. J. Appl. Earth Obs. Geoinf.* **2019**, *82*, 101920. [CrossRef]

40. Liu, Y.; Huang, J.; Xie, D.; Huang, S.; Ying, C.; Li, L. Impact of SSC distribution in Hangzhou Bay after 1307 typhoon through satellite images. *Hydro-Sci. Eng.* **2021**, *6*, 9–16.

41. Huang, J.; Yuan, R.; Zhu, J. Numerical Simulation and Analysis of Water and Suspended Sediment Transport in Hangzhou Bay, China. *J. Mar. Sci. Eng.* **2022**, *10*, 1248. [CrossRef]

42. Zhu, L.; Huang, Y.; Yang, G.; Sun, W.; Chen, C.; Huang, K. Information extraction and spatio-temporal evolution analysis of the coastline in Hangzhou Bay based on Google Earth Engine and remote sensing technology. *Remote Sens. Nat. Resour.* **2023**, *35*, 50–60.

43. Wang, S.; Xu, M.; Han, Y.; Gao, G.; Huang, H. Analysis and scenario prediction of multi-year blue carbon in intertidal wetland on the south bank of Hangzhou Bay. *China Environ. Sci.* **2022**, *42*, 4380–4388.

44. Fang, Q.; Huang, S.; Xu, X.; Wang, J.; Li, D.; Xie, H. Analysis of the influence of reclamation engineering group on the accumulated hydrodynamics in the south coast of Hangzhou Bay. *Sci. Technol. Eng.* **2020**, *20*, 5338–5344.

45. Li, L.; Ren, Y.; Ye, T.; Wang, X.H.; Huang, J.; Xia, Y. Positive feedback between the tidal flat variations and sediment dynamics: An example study in the macro-tidal turbid Hangzhou Bay. *J. Geophys. Res.-Ocean.* **2023**, *128*, e2022JC019414. [CrossRef]

46. Tian, Q.; Zheng, L.; Tong, Q. Atmospheric radiation correction and reflectance inversion method based on remote sensing imagery. *J. Appl. Meteorol. Sci.* **1998**, 77–82.

47. Gens, G. Remote sensing of coastlines: Detection, extraction and monitoring. *Int. J. Remote Sens.* **2010**, *31*, 1819–1836. [CrossRef]

48. Awange, J.; Saleem, A.; Sukhadiya, R.; Ouma, Y.; Kexiang, H. Physical dynamics of Lake Victoria over the past 34 years (1984–2018): Is the lake dying? *Sci. Total Environ.* **2019**, *658*, 199–218. [CrossRef] [PubMed]

49. Amos, C.L. Chapter 10 Siliciclastic Tidal Flats. *Dev. Sedimentol.* **1995**, *53*, 273–306.

50. Zhang, Y.; Gao, Z.; Liu, X.; Xu, N. The extraction method of tidal flat area based on remote sensing waterlines. *Ocean Dev. Manag.* **2018**, *35*, 56–61.

51. Han, Z.; Guo, Y. Waterside line information extraction of tidal flat at the Yangtze River Estuary by wavelet multi-resolution analysis. *Mar. Sci.* **2011**, *35*, 67–70.

52. Li, X.; Zhang, H. Edge detection algorithm of gray image. *Electron. Opt. Control* **2018**, *25*, 46–49.

53. Dong, Z.; Fu, D.; Liu, D.; Yu, G.; Zhang, X. Study on the extraction of waterline with different landforms based on ZY-3 remote sensing images. *Hydrogr. Surv. Charting* **2019**, *39*, 34–39.

54. Luo, M.; Zhang, D. Research on accurate extraction of waterline under conditions of blurred water-land boundary. *Mar. Sci.* **2019**, *43*, 106–112.

55. Bi, J.; Zhang, L.; Wang, P.; Sui, Y.; Mu, X.; Wang, P. Improved mathematical morphology-based image segmentation algorithm for coastline extraction and its region adaptability analysis. *Geogr. Geo-Inf. Sci.* **2019**, *35*, 20–29.

56. Yan, H.; Li, B.; Chen, M. Progress of researches in coastline extraction based on RS technique. *Areal Res. Dev.* **2009**, *28*, 101–105.

57. Egbert, G.D.; Erofeeva, S.Y. Efficient Inverse Modeling of Barotropic Ocean Tides. *J. Atmos. Ocean. Technol.* **2002**, *19*, 183–204. [CrossRef]

58. Hua, Y. *Study on the Expansion of Reclamation and Land Use Changes in Hangzhou Bay*; Zhejiang University: Zhejiang, China, 2016.

59. Zhang, X.; Zhang, X.; Yang, B.; Zhuang, Z.; Shang, K. Coastline extraction using remote sensing based on coastal type and tidal correction. *Remote Sens. Land Resour.* **2013**, *25*, 91–97.

60. Chen, W.; Zhang, D.; Cui, D.; Lv, L.; Xie, W.; Shi, S.; Hou, Z. Monitoring spatial and temporal changes in the continental coastline and the intertidal zone in Jiangsu province, China. *Acta Geogr. Sin.* **2018**, *73*, 1365–1380.

61. Sha, H.; Zhang, D.; Cui, D.; Lv, L.; Ni, P. Remote sensing prediction method of coastline based on self-adaptive profile morphology. *Acta Oceanol. Sin.* **2019**, *41*, 170–180.

62. Liu, Y.; Cong, P.; Li, J.; Wei, B.; Dai, J.; Han, C. A morphological analysis of tidal creek in the Yellow River Delta based on remote sensing. *Mar. Environ. Sci.* **2020**, *39*, 393–398.

63. Huete, A.; Didan, K.; Marani, M.; Rodriguez, E.P.; Gao, X.; Ferreira, L.G. Overview of the radiometric and biophysical performance of the MODIS vegetation indices. *Remote Sens. Environ.* **2002**, *83*, 195–213. [CrossRef]

64. Arthur, S. Dynamic basis of geomorphology. *Geol. Soc. Am. Bull.* **1952**, *63*, 923–938.

65. Meng, M.; Tian, H.; Wu, M.; Wang, L.; Niu, Z. Analysis of the Evolution of Wetland Landscape Spatial Pattern Based on Google Earth Engine Platform: Taking Baiyangdian as an Example. *J. Yunnan Univ. Nat. Sci. Ed.* **2019**, *41*, 416–424.

66. Lin, S. *Study on Water Information Extraction Method of GF-1 Image Based on the Combination of NDVI and Modified FCM*; Geomatics & Spatial Information Technology: Harbin, China, 2017.

67. Dubey, Y.; Mushrif, M.; Mitra, K. Brain tumor detection and segmentation using multiscale intuitionistic fuzzy roughness in MR images. *Biomed. Eng. -Appl. Basis Commun.* **2019**, *31*, 1950020. [CrossRef]

68. Chen, H.; Chen, C.; Zhang, Z.; Wang, L.; Liang, J. A remote sensing information extraction method for intertidal zones based on Google Earth Engine. *Remote Sens. Nat. Resour.* **2022**, *34*, 60–67.

69. Horton, R.E. Erosional development of streams and their drainage basins: Hydrophysical approach to quantitative morphology. *Bull. Geol. Soc. Am.* **1945**, *56*, 275–370. [CrossRef]

70. Hao, X. *Study on the Morphological Characteristics and Evolution of Tidal Trenches on the Land Shore of Jiangsu Radiation Sandbar*; Nanjing Normal University: Nanjing, China, 2021.

71. Liu, Y.; Li, J.; Zhang, Y.; Zhao, X.; Xu, W.; He, G.; Liu, Y. Dynamic monitoring of vegetation in Southern Hangzhou Bay from time series images. *J. Ningbo Univ. (Nat. Sci. Eng. Ed.)* **2020**, *30*, 25–31.

72. Pettorelli, N.; Vik, J.O.; Mysterud, A.; Gaillard, J.; Tucker, C.; Stenseth, N. Using the satellite-derived NDVI to assess ecological responses to environmental change. *Trends Ecol. Evol.* **2005**, *20*, 503–510. [CrossRef] [PubMed]

73. Carol, A.; Wilson, Z.; FitzGerald, D.; Hopkinson, C.; Valentine, V.; Kolker, A. Saltmarsh pool and tidal creek morphodynamics: Dynamic equilibrium of northern latitude saltmarshes? *Geomorphology* **2014**, *213*, 99–115.

74. Kearney, W.S.; Fagherazzi, S. Salt marsh vegetation promotes efficient tidal channel networks. *Nat. Commun.* **2016**, *7*, 12287. [CrossRef]

75. Ye, M.; Li, J.; Shi, X.; Jiang, Y.; Shi, Z.; Xu, L.; He, G.; Huang, R.; Feng, B. Spatial pattern change of the coastline development and utilization in Zhejiang from 1990 to 2015. *Geogr. Res.* **2017**, *36*, 1159–1170.

76. Ren, Y. *Characteristics and Mechanism of Suspended Sediment in Hangzhou Bay Considering Wave-Current Interaction*; Zhejiang University: Zhejiang, China, 2022.

77. Zheng, X.; Zhou, B.; Lei, H.; Huang, Q.; Ye, H. Extraction and spatio-temporal change analysis of the tidal flat in Cixi section of Hangzhou Bay based on Google earth engine. *Remote Sens. Nat. Resour.* **2022**, *34*, 18–26.

78. Jafari, R.; Sui, J. Velocity Field and Turbulence Structure around Spur Dikes with Different Angles of Orientation under Ice Covered Flow Conditions. *Water* **2021**, *13*, 1844. [CrossRef]

79. Dai, Z.; Liu, J. Impacts of large dams on downstream fluvial sediment: An example of the Three Gorges Dam (TGD) on the Changjiang (Yangtze River). *J. Hydrol.* **2013**, *480*, 10–18. [CrossRef]

80. Dai, Z.; Liu, J.; Wei, W.; Chen, J. Detection of the Three Gorges Dam influence on the Changjiang (Yangtze River) submerged delta. *Sci. Rep.* **2014**, *4*, 6600. [CrossRef] [PubMed]

81. Xie, D.; Pan, C.; Cao, Y.; Zhang, B. Decadal variations in the erosion/deposition pattern of the Hangzhou Bay and their mechanism in recent 50a. *Haiyang Xuebao* **2013**, *35*, 121–128+9.

82. Fu, Y.; Yin, P.; Gao, F.; Liu, D.; Cao, K.; Tian, Y. Remote sensing study on Spartina alterniflora in the northern tidal flat of Sanmen Bay in Zhejiang Province. *Period. Ocean Univ. China* **2002**, *52*, 134–144.

83. Lou, Y.; Dai, Z.; Long, C.; Dong, H.; Wei, W.; Ge, Z. Image-based machine learning for monitoring the dynamics of the largest salt marsh in the Yangtze River Delta. *J. Hydrol.* **2022**, *608*, 127681. [CrossRef]